Manipulation of Heterogeneous Surface Electric Potential Promotes Osteogenesis by Strengthening RGD Peptide Binding and Cellular Mechanosensing

Yunyang Bai, Xiaona Zheng, Xianwei Zhong, Qun Cui, Shuan Zhang, Xiufang Wen, Boon Chin Heng, Shan He, Yang Shen, Jinxing Zhang, Yan Wei,* Xuliang Deng,* and Xuehui Zhang*

The heterogeneity of extracellular matrix (ECM) topology, stiffness, and architecture is a key factor modulating cellular behavior and osteogenesis. However, the effects of heterogeneous ECM electric potential at the micro- and nanoscale on osteogenesis remain to be elucidated. Here, the heterogeneous distribution of surface potential is established by incorporating ferroelectric BaTiO$_3$ nanofibers (BTNF) into poly(vinylidene fluoridetrifluoroethylene) (P(VDF-TrFE)) matrix based on phase-field and first-principles simulation. By optimizing the aspect ratios of BTNF fillers, the anisotropic distribution of surface potential on BTNF/P(VDF-TrFE) nanocomposite membranes can be achieved by strong spontaneous electric polarization of BTNF fillers. These results indicate that heterogeneous surface potential distribution leads to a meshwork pattern of fibronectin (FN) aggregation, which increased FN-III7-10 (FN fragment) focal flexibility and anchor points as predicted by molecular dynamics simulation. Furthermore, integrin clustering, focal adhesion formation, cell spreading, and adhesion are enhanced sequentially. Increased traction of actin fibers amplifies mechanotransduction by promoting nuclear translocation of YAP/Runx2, which enhances osteogenesis in vitro and bone regeneration in vivo. The work thus provides fundamental insights into the biological effects of surface potential heterogeneity at the micro- and nanoscale on osteogenesis, and also develops a new strategy to optimize the performance of electroactive biomaterials for tissue regenerative therapies.

1. Introduction

Physical properties of biomaterials, such as stiffness, topological structure, and electricity, play critical roles in regulating cell behavior and tissue function.[1] At the micro- and nanoscale levels, biological tissues are composed of heterogeneous distributions of cells and various architectural elements of the extracellular matrix (ECM). Specifically, mesenchymal stem cells (MSCs) reside in an ECM niche microenvironment in the form of an anisotropic fibrous scaffold.[2] Heterogeneity is considered a basic feature of ECM, and numerous studies have demonstrated that cell behavior and stem cell fate are strongly influenced by the physical heterogeneity of matrix materials.[3]
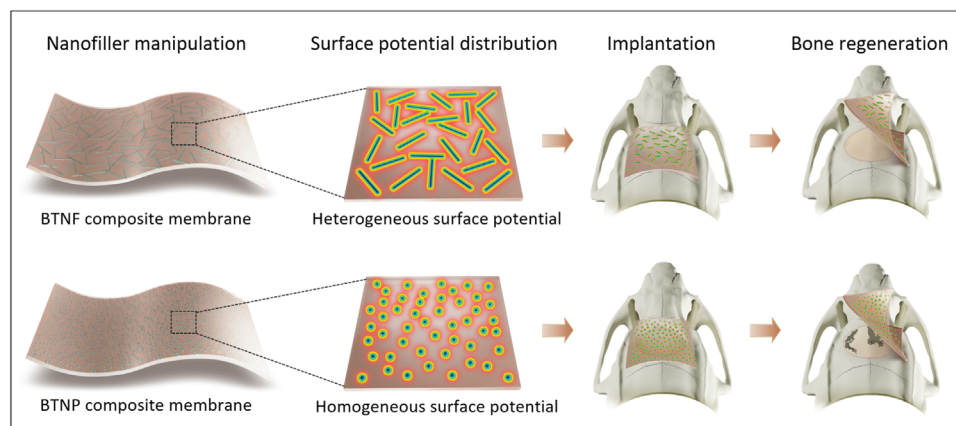
Charged biomaterials have received increasing attention in the biomaterial research field in recent years.[4] In particular, ferroelectric materials, including polyvinylidene fluoride (PVDF) and its copolymer P(VDF-TrFE),[5] barium titanate (BaTiO$_3$, BTO),[6] lithium niobate (LN),[7] and sodium potassium citrate (KNN),[8] etc., have been widely investigated as

Y. Bai, X. Zheng, Q. Cui, Y. Wei, X. Deng, X. Zhang
NMPA Key Laboratory for Dental Materials
National Engineering Research Center of Oral Biomaterials and Digital
Medical Devices
Beijing Laboratory of Biomedical Materials
Beijing Key Laboratory of Digital Stomatology
Peking University School and Hospital of Stomatology
Beijing 100081, P. R. China
E-mail: kqweiyan@bjmu.edu.cn; kqdengxuliang@bjmu.edu.cn;
zhangxuehui@bjmu.edu.cn

Y. Bai, X. Zheng, Y. Wei, X. Deng
Department of Geriatric Dentistry
Peking University School and Hospital of Stomatology
Beijing 100081, P. R. China

X. Zhong, S. Zhang, X. Wen
The School of Chemistry and Chemical Engineering
South China University of Technology
Guangzhou 510640, P. R. China

Q. Cui, X. Zhang
Department of Dental Materials & Dental Medical Devices Testing Center
Peking University School and Hospital of Stomatology
Beijing 100081, P. R. China

B. C. Heng
Central Laboratory
Peking University School and Hospital of Stomatology
Beijing 100081, P. R. China

Scheme 1. Illustration of manipulating surface electric potential heterogeneity on BTO/P(VDF-TrFE) ferroelectric nanocomposites to promote bone regeneration. By turning the dimension and aspect ratios of BTO nanofillers, a line-like anisotropic distribution of surface electric potential is observed on the BTO nanofibers/P(VDF-TrFE) (BTNF) nanocomposite membrane after poling polarization, in contrast to the high-potential homogeneous pitting distribution on the BTO nanoparticles/P(VDF-TrFE) (BTNP) composite membrane. After implantation to cover supercritical-sized calvarial defects (8 mm) in mature rats, the polarized BTNF composite membrane facilitated improved new bone formation that led to almost complete healing with full bone maturity after 12 weeks post-implantation, which is mediated by the heterogeneous surface electric potential microenvironment. By contrast, for the control covered with polarized BTNP membranes, there was a lack of complete and continuous nascent bone formation within the defect site after 12 weeks post-implantation.

biomimetic materials that simulate the electric microenvironment at the macroscale for bone tissue engineering applications, due to their spontaneous electric polarization properties. Nevertheless, the effects of heterogeneous electric potential of matrix materials at the micro- and nanoscale scales on cellular behavior and osteogenesis remain to be elucidated. This represents a dire gap in scientific knowledge, as under natural physiological conditions, electrical heterogeneity is considered to more closely resemble the electrical microenvironment of ECM.[9] Hence, it is imperative to explore the effects of biomaterials with heterogeneous electrical charge distribution on cell or tissue behavior at the micro- and nanoscale levels. These results might provide essential information for optimizing the electrical properties of implant materials to improve the efficacy of bone regeneration.

Hence, this study attempted a proof-of-concept validation of osteogenesis being enhanced by heterogeneous surface electric potential distribution of ferroelectric nanocomposite membranes. The heterogeneous distributions of surface electrical potential was established by incorporating ferroelectric BaTiO$_3$ nanofibers (BTNF) into poly(vinylidene fluoride trifluoroethylene) (P(VDF-TrFE)) matrix. By optimizing the aspect ratios of BTNF fillers, the anisotropic distribution of surface potential on BTNF/P(VDF-TrFE) nanocomposite membrane could be achieved by the strong spontaneous electric polarization of BTNF fillers (**Scheme 1**). More fibronectin (FN) anchor points are con-

centrated on the areas occupied by BTNF fillers, as evidenced by molecular dynamic (MD) simulation, thereby contributing to a meshwork pattern of fibronectin adsorption on the membrane surface with heterogeneous electrical potential distribution. This protein adsorption pattern not only enhanced the adhesion and spreading of bone marrow mesenchymal stem cells (BM-MSCs), but also increased the traction force on actin fibers connected to focal adhesions, which amplified mechanotransduction by promoting nuclear translocation of yes-associated protein/runt-related transcription factor 2 (YAP/Runx2). This in turn promoted osteogenic differentiation of BM-MSCs in vitro and bone regeneration in vivo.
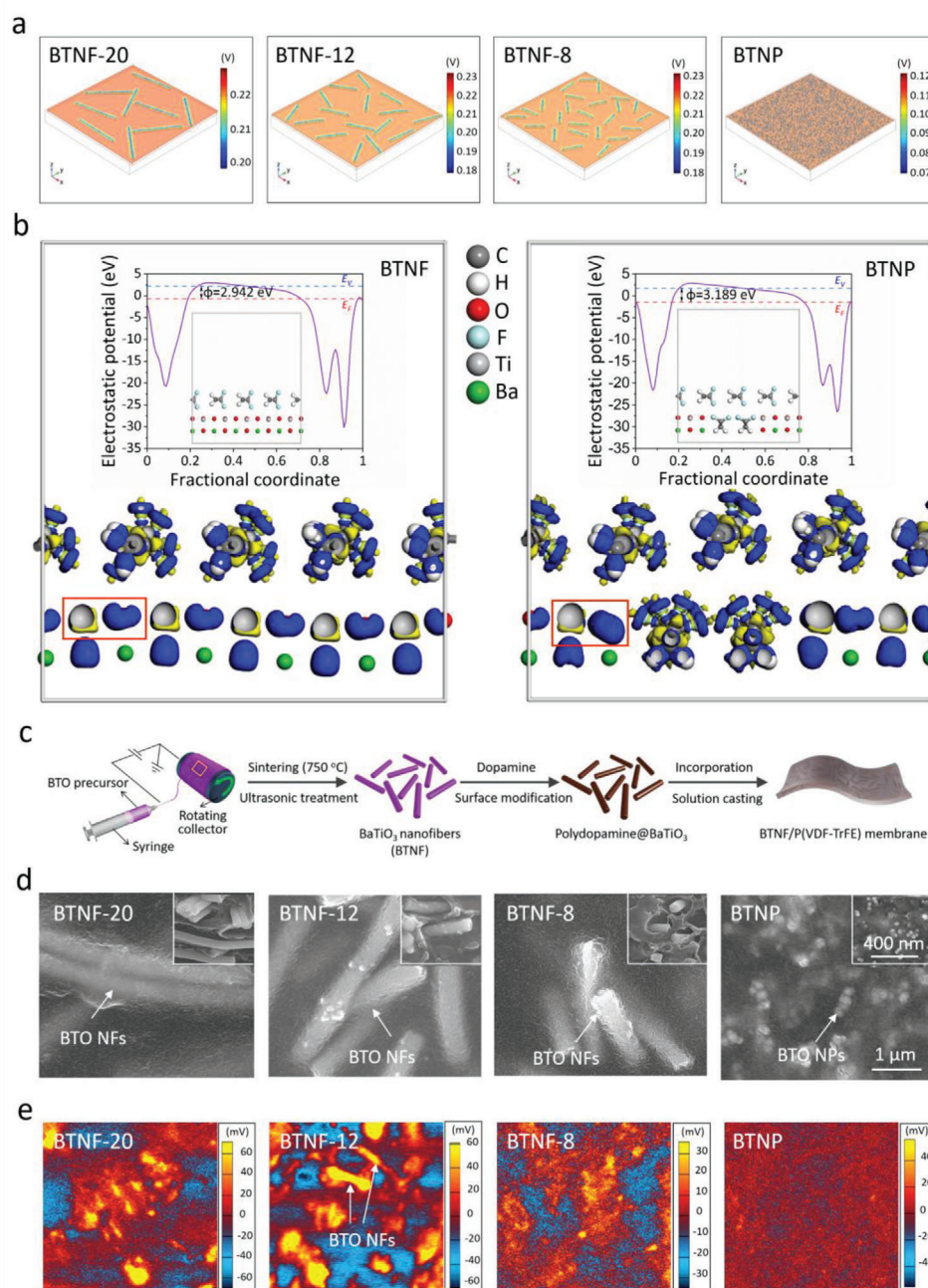
2. Results and Discussion

2.1. Theoretical Simulation of Surface Potential Distribution on Ferroelectric Nanocomposite Membranes

To predict the heterogeneous surface potential distribution on ferroelectric nanocomposite membranes, theoretical models based on phase-field simulation were constructed. The ferroelectric BTO/P(VDF-TrFE) nanocomposite membranes with a variety of different nanofillers, including nanofibers with different aspect ratios (ARs, BTNF-20, BTNF-12, and BTNF-8, respectively) or nanoparticles with diameter of 100 nm were designed for phase-field simulation. Within the simulation models (**Figure 1**a), the surface electrical potential of the polymer matrix is consistently higher than that of the BTO nanofillers. The concentration of surface electrical potential on the polymer matrix could be attributed to large differences in the dielectric constants of BaTiO$_3$ and P(VDF-TrFE).[10] BTNFs induce a more substantial concentration of local electric field in their vicinity compared to their spherical counterparts, because the surface area of BTNFs is far larger than BTNPs. Another reason for the concentrated surface electrical potential on the fiber-filled composites

S. He, Y. Shen
School of Materials Science and Engineering
State Key Lab of New Ceramics and Fine Processing
Tsinghua University
Beijing 100084, P. R. China

J. Zhang
Department of Physics
Beijing Normal University
Beijing 100875, P. R. China

Figure 1. The theoretical simulation and establishment of heterogeneous surface potential distribution on ferroelectric nanocomposite membranes. a) The theoretical models of surface potential distribution on ferroelectric nanocomposite membranes incorporated with nanofibers with different aspect ratios or nanoparticle fillers based on phase-field simulitions. b) First-principles calculation of the charge density difference between BTNF (left) and BTNP (right). The blue and yellow are charge depletion and accumulation, respectively. The red squares denote that the charge density change of Ti atoms and O atoms in BTO nanoparticles is much greater than that in the BTO nanofibers. The insets show the electrostatic potentials of BTNF and BTNP. The orange and blue dashed lines are the fermi and vacuum energy level, respectively. c) Schematic diagram of the BTNF/P(VDF-TrFE) composite membrane fabrication process. d) Representative SEM images of the nanocomposite membranes. The insets showed the cross-sectional observation. The white arrows denote the BTO nanofibers or BTO nanoparticles. e) Representative SKPM images of nanocomposite membranes with BTNF-20, BTNF-12, BTNF-8, or BTNP fillers. The white arrows denote the BTO nanofibers.

**ADVANCED
SCIENCE NEWS**

www.advancedsciencenews.com

**ADVANCED
MATERIALS**

www.advmat.de

may lie in the large aspect ratio of BTNFs. Overall, the simulation results show that a high local surface potential distribution can be obtained by increasing the aspect ratio of BTNFs fillers. The fibers with favorable properties constitute a network of specific surface electrical potential. Results of our previous phase-field simulations indicate that fibers with large aspect ratios exhibit substantial dielectric anisotropy along their longitudinal or radial directions.[11] When oriented with their longitudinal directions aligned to the in-plane directions of the composite membranes, the BTNFs induce substantially concentrated local electric fields at their corners. Spherical particles, on the other hand, result in much less concentration of the local electric field.

To further predict and analyze the difference in surface potential between BTNF and BTNP, first-principles simulation was performed to clarify the charge density difference between BTO nanofibers and BTO nanoparticles. As shown in the red square of Figure 1b, the charge density difference between Ti atoms and O atoms in BTO particles is much greater than that in BTO fibers, indicating that more charge transfer of BTO particles will occur after the heterojunction with P(VDF-TrFE). The calculated Hirshfeld charge of BTNF and BTNP is 0.65 and 0.09 e, respectively, indicating that the P(VDF-TrFE) layer potential is positive with the addition of BTO fiber and BTO particle, and that the surface potential of BTNF is higher than that of BTNP (Figure S3, Supporting Information). Furthermore, the work function ϕ was quantified to characterize the electron transfer between P(VDF-TrFE) and BTO nanofibers or BTO nanoparticles. Electrons will flow from the lower work function to the higher work function when two substances with different work functions contact each other, resulting in different electron concentrations and potentials on both sides.[12] In this study, the work function ϕ of P(VDF-TrFE) (Figure S1, Supporting Information), BTNF and BTNP (the insets in Figure 1b) were 7.274, 2.942, and 3.189 eV, respectively. This clearly shows that the work function of BTNF is lower than that of BTNP, after the formation of heterojunction between P(VDF-TrFE) and BTO nanofibers or BTO nanoparticles, indicating that the electron generating capacity of BTNF is lower than that of BTNP. These simulation results predicted that the surface potential at the interface between the BTO nanofiber fillers and the P(VDF-TrFE) matrix will be higher than that of the BTO nanoparticle fillers. These simulation results thus suggest that transforming the dimension of the BTO nanofiller, while retaining the same material composition can not only achieve a heterogeneous distribution of surface potential, but can also achieve an optimal electric potential level on the material surface.

2.2. Designing and Establishing Heterogeneous Surface Electric Potential Distribution on Ferroelectric Nanocomposite Membranes

Based on the theoretical simulations, we utilized a strategy to manipulate the filler dimensions from 0D BaTiO$_3$ nanoparticles (BTNP, Figure S4a, Supporting Information) to 1D BaTiO$_3$ nanofibers (BTNF, Figure S4b, Supporting Information) within the P(VDF-TrFE) matrix, utilizing the same filler material content. First, BTNF was prepared by electrospinning (Figure 1c) and an optimal pure cubic phase structure similar to BTNP was achieved by tailing the sintering temperature, as confirmed by

X-ray diffraction (XRD) patterns (Figure S4g, Supporting Information). Surface modification of the nanofillers by polydopamine was confirmed by HR-TEM images (Figure S4c–f, Supporting Information) and XPS patterns (Figure S4h–j, Supporting Information), which could improve compatibility at the filler/matrix interface and also facilitate covalent bonding between ceramics fillers and the polymer matrix.[13]

We utilized ultrasonication treatment as a universal strategy to control the aspect ratios of BTO nanofiber fillers. The BTO nanofiber fillers with different aspect ratios (ARs, BTNF-20, BTNF-12, and BTNF-8, respectively) (Figure S6, Supporting Information) were obtained by adjusting the ultrasonication time (for 1, 5, and 15 min, respectively), and were used to optimize the heterogeneous distribution of surface potential on the nanocomposite membrane. From the results of the FE-SEM images (Figure 1d), the orientation of BTO nanofibers along the in-plane direction of the polymer matrix can be readily distinguished, whereas BTNP is dispersed within the polymer matrix isotropically. We further investigated the distribution of BTNF-20, BTNF-12, and BTNF-8 nanofillers within the polymer matrix through cross-sectional observation (the insets in Figure 1d; Figure S5a, Supporting Information). It was found that the fibers are stacked in parallel within the matrix when the fibers are too long (i.e., BTNF-20), while the filler did not exhibit obvious heterogeneous distribution within the matrix when the fibers are too short (i.e., BTNF-8), which is similar to the distribution of BTNPs. Interestingly, the BTNF fillers exhibited optimal dispersion and the expected anisotropic distribution in BTNF-12 (Figure 1d), and formed a tight bond with the polymer matrix (Figure S5a, Supporting Information), which provided a topological basis for the establishment of surface potential heterogeneity. The presence of BTO nanofibers and nanoparticles in the P(VDF-TrFE) matrix was further confirmed by EDS spectra (Figure S5b,c, Supporting Information), XRD patterns (Figure S5d, Supporting Information) and ATR-FTIR spectra (Figure S5e, Supporting Information).

The phase-field simulations are confirmed by testing of surface electric potential based on scanning Kelvin probe microscopy (SKPM) imaging (Figure 1e). Interestingly, a line-like anisotropic distribution of surface electric potential is clearly observed on BTNF-12, while BTNF-20 and BTNF-8 composite membrane surfaces exhibited no obvious surface potential heterogeneity distribution. This is directly related to differences in the distribution of fiber fillers with different aspect ratios in the polymer matrix. We have also observed that the BTNP composite membrane surface has a high-potential homogeneous pitting distribution, which is in sharp contrast to the heterogeneous surface potential distribution on the BTNF-12 composite membrane. This difference may be due to the local surface potential increase being caused by different shapes of the BTO filler after polarization treatment,[11b,14] which fully confirmed the first-principles simulation results.

Furthermore, the effects of other physico-chemical properties, including surface roughness, surface wettability, surface energy, and mechanical performance (elastic modulus, tensile strength, and hardness) of the composites were also characterized, with no significant differences among the four types of composite membranes being observed (Table S2, Supporting Information). This thus enabled us to focus exclusively on the effects of surface

electrical potential distribution on the biological properties of the composites, excluding interference from other general physico-chemical properties.

2.3. Heterogeneous Surface Potential Distribution Actuates Heterogeneous Meshwork Pattern of Fibronectin Adsorption

Subsequently, we investigated how the amount and distribution patterns of protein adsorption is affected by the heterogeneous surface potential. As shown in **Figure 2**a, the adsorption of FN on the BTNF-12 composite membrane surface exhibits a heterogeneous meshwork pattern after 6 h of immersion, whereas the other two types of BTNF membranes and BTNP membranes yielded dense and uniform FN absorption. Quantitatively, the BTNF-12 composite membranes exhibited the largest amount of FN adsorption, as compared to the other membranes after 6 h of immersion (Figure 2d), which was also confirmed by micro-BCA analysis of the total FN adsorption contents (Figure 2e). This difference is closely related to the uniformity of the electric field distribution on the surface of the composite membrane. As explained by our previous studies,[11] the BTNFs induce more substantial heterogeneous electric potential distribution in their vicinity compared to their spherical counterparts. The concentrated local electric potential at the corners of BTNFs will lead to more protein adsorption,[15] which enables the heterogeneous surface potential distribution of nanocomposite membranes to have a much higher protein adsorption capacity compared to BTNP membranes. Given the larger specific surface area of BTNFs compared to BTNPs, the BTNFs are capable of inducing more substantial interfacial polarization at the same volume fraction of the polymer matrix.[11] The enhanced interfacial polarization causes the protein to be adsorbed in a meshwork-like pattern, as well as led to significantly higher levels of adsorption due to higher electrical charge density that results in stronger attraction to charged amino acid residues on the protein.[15a]

To gain an in-depth understanding of the initial stereoselectivity between the nanocomposite membrane and adhesive ligands, classical molecular dynamic (MD) simulations modeled on FN-III7-10, as the key cell-binding domains of fibronectin (FN) were performed.[16] Within the simulation models, the BTNF nanocomposite membrane exhibited greater numbers of absorbed residues than that of the BTNP nanocomposite membrane (Table S3, Supporting Information), which indicates that FN adsorbed on the surface of the BTNF composite membrane with stronger affinity. Interestingly, the BTNF-12 nanocomposite membrane exhibited minimal distance between the FN-III7-10 protein and nanocomposite membrane in the first 2000 ps of MD simulation (Figure S7, Supporting Information), thus indicating that the FN-III7-10 protein was initially stably adsorbed on the surface of the BTNF-12 nanocomposite membrane. The enhanced FN-III7-10 protein adsorption by BTNF-12 nanocomposite membrane was also supported by the highest value of interaction energy (Figure S8, Supporting Information). It was also found that the electrostatic interaction was the main driving force of the protein adsorption process.

The ARG-Gly-ASP (RGD) sequence in FN plays a pivotal role in mediating cell adhesion due to its specific recognition of the extra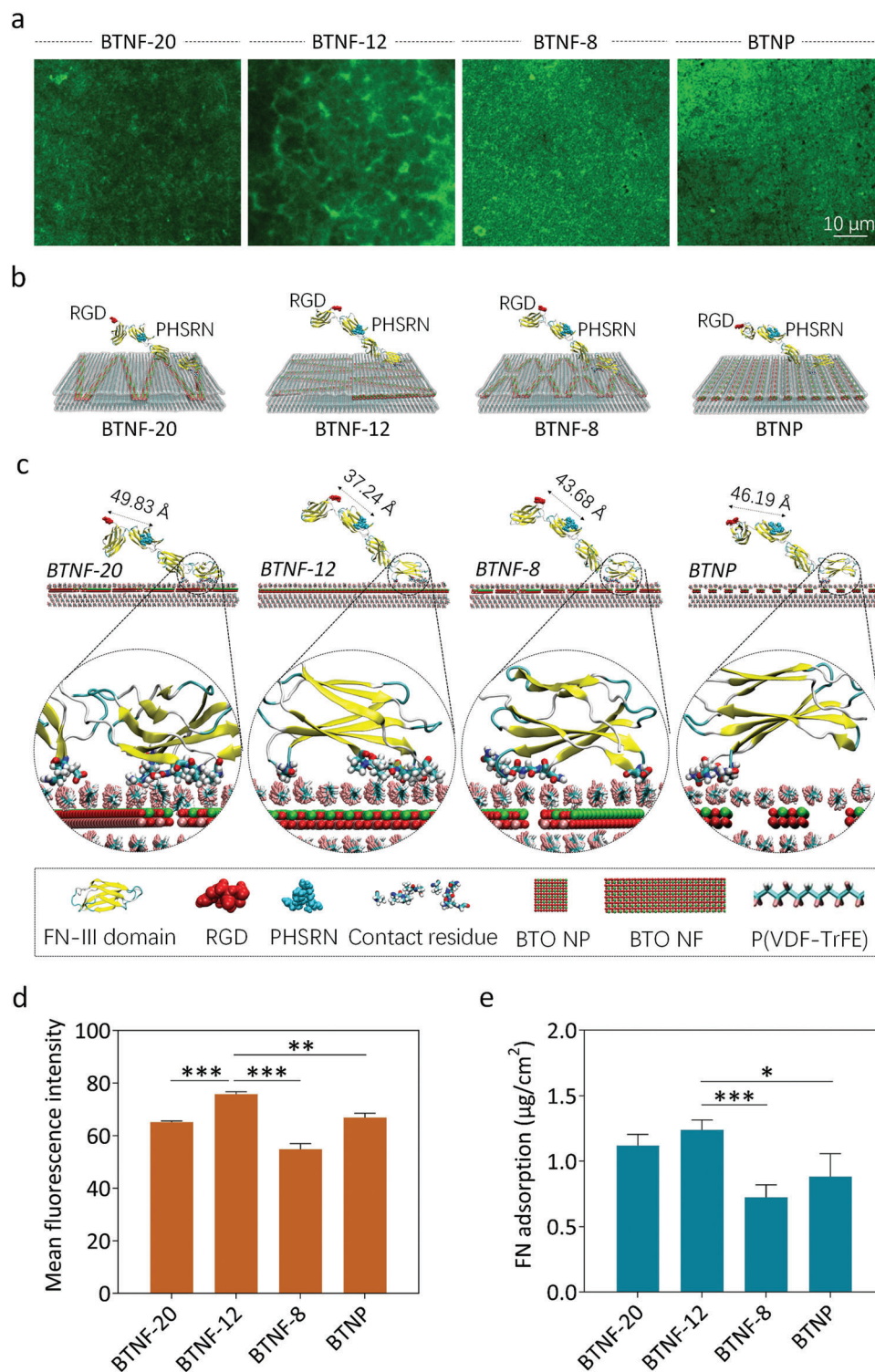cellular domain of the integrin receptor.[17] As reported, a 35 Å distance between RGD and PHSRN is most suitable for the binding of integrin to FN.[18] The distance between RGD and PHSRN residues on the BTNF-12 membrane surface is 37.24Å (Figure 2c), which is close to 35 Å, indicating that the BTNF-12 membrane surface can promote FN adsorption and that its RGD sequence affinity can facilitate cell recognition and subsequent functions. Furthermore, we observed most FN anchor points and optimal FN conformation on the BTNF-12 membrane from the 3D view of molecular dynamic simulations (Figure 2b). From the experimental and MD simulation results, we can surmise that the BTNF-12 nanocomposite membrane provides a favorable microenvironment for protein adsorption, resulting in positive cell recognition, adhesion and functional differentiation.

In the following studies, we will thus focus on the BTNF-12 composite membrane as a material model of heterogeneous surface potential distribution. The macroscopic electrical properties of the BTNF nanocomposite membrane was also evaluated and it was found that the piezoelectric coefficient (d_{33}) of the BTNF membrane ($\approx$7.91 pC N^{-1}) is similar to that of natural bone,[19] which remained stable at >90% of its original value for up to 21 days under simulated physiological conditions (Figure S5f, Supporting Information). This outstanding electrical stability could enable BTNF nanocomposite membranes to maintain a local heterogeneous electric microenvironment and may exert a positive effect in promoting osteogenesis.

2.4. Heterogeneous Surface Potential Distribution Promotes Initial Cell Response
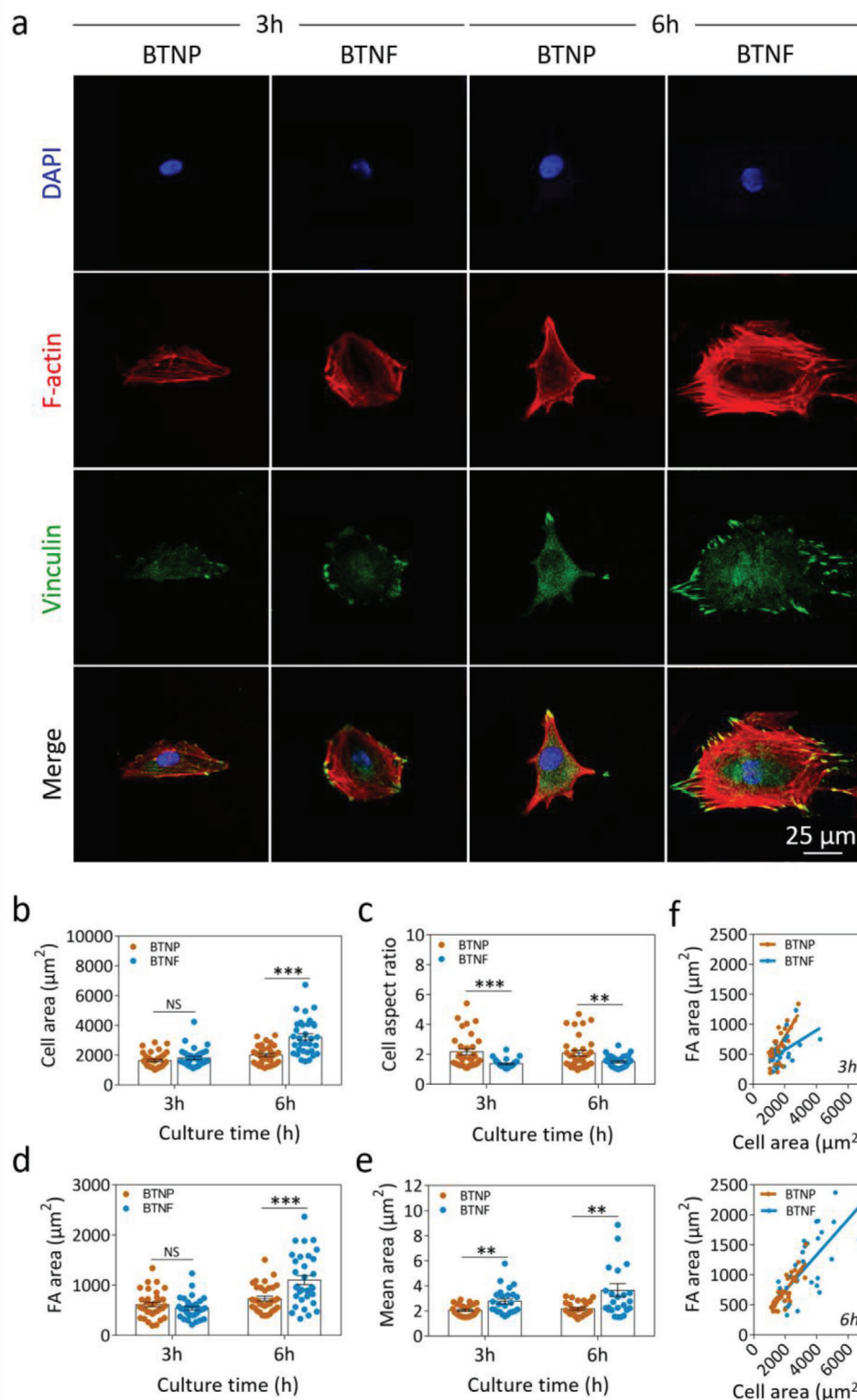
We next evaluated differences in the initial cell response to surfaces with different electric potential distribution. Representative SEM images show that BM-MSCs exhibited a polygonal shape with numerous lamellipodia extending onto the BTNF membranes at 6 h post-seeding (Figure S9, Supporting Information). By contrast, only a few obvious lamellipodia extended from the cell onto the BTNP membrane surfaces. Cells possess large-sized protrusions, such as lamellipodia, that are driven by a network of dynamic contractile machinery, which are essential for cellular adhesion, polarization, and spreading.[20] Interestingly, adherent cells appear to possess more sub-micrometer or even nanometer-sized filopodia on the BTNF substrates, as compared to the BTNP substrates (Figure S9, Supporting Information). This phenomenon may be explained by the fact that cells respond more strongly to special stimuli from the heterogeneous surface electric domains, inducing them to actively perceive and respond to this novel microenvironmental feature, thereby continuously stretching the cell bodies, which would in turn exert a positive effect on the functional differentiation of stem cells.[21] Hence, we hypothesize that charged substrate surfaces with different electric potential distribution induce differential organization of cell adhesion and remodeling of cytoskeletal structures.

After 6 h of co-culture, confocal microscopy showed that the BM-MSCs cultured on the BTNF substrates exhibited more abundant cytoskeletal organization (**Figure 3**a) and significantly larger cell spreading area (Figure 3b), as compared to the BTNP substrates (3219.74 ± 1188.24 μm^2 on BTNF and 1995.95 ± 609.00 μm^2 on BTNP, respectively). The quantitative analysis of cell aspect ratio (Figure 3c) showed that the elongation of cells

**ADVANCED
SCIENCE NEWS**

www.advancedsciencenews.com
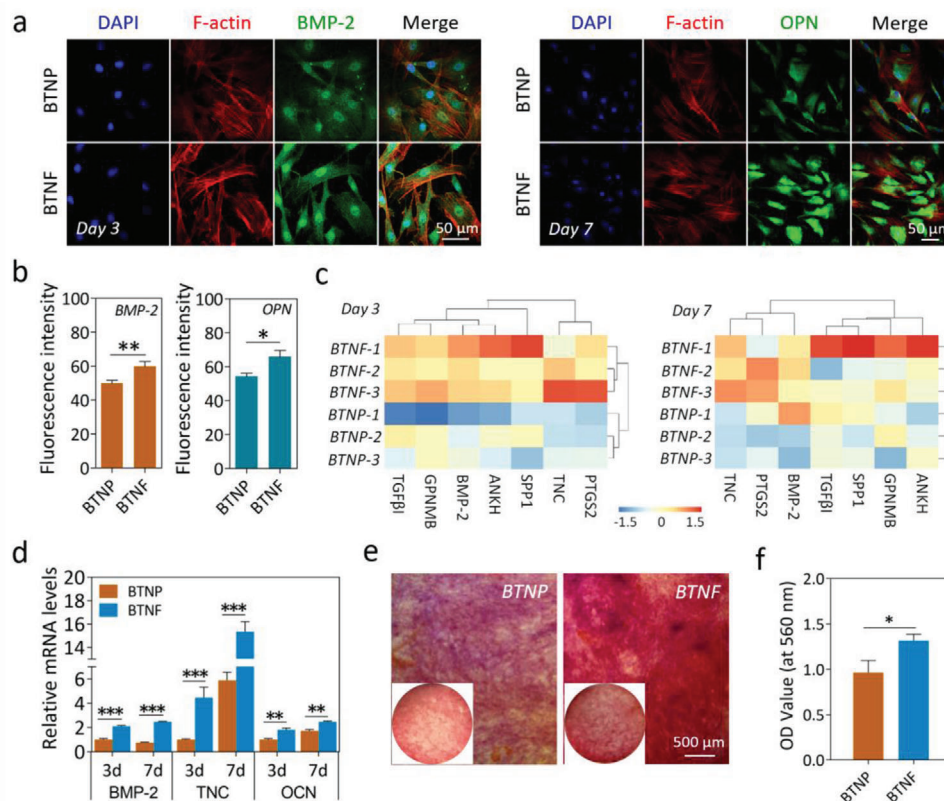
**ADVANCED
MATERIALS**

www.advmat.de

Figure 2. Manipulation of heterogeneous surface potential distribution actuates fibronectin (FN) adsorption. a) Immunofluorescence staining images of FN adsorption after 6 h of incubation. b) 3D view of molecular dynamic simulations of FN-III7-10 adsorbed on the different nanocomposite membranes surfaces after 20 ns. c) The conformational change of FN-III7-10 adsorbed on the different nanocomposite membranes surfaces after 20 ns molecular dynamic simulation. The distance between RGD and PHSRN on BTNF-12 nanocomposite membrane is more close to 35 Å, which is considered the most suitable for binding of integrin $\alpha 5\beta 1$ to FN. d) Quantitative analysis of the fluorescence intensity of FN adsorption at 6 h after incubation. e) Micro-BCA analysis of FN adsorption after 6 h of incubation. (NS, not significant; $^*p < 0.05$; $^{**}p < 0.01$ and $^{***}p < 0.001$.)

Figure 3. Heterogeneous surface potential distribution promotes cell-scaffold interaction. a) Representative immunofluorescence images of focal adhesions (FAs, green), actin network (Phalloidin, red), and cell nuclei (DAPI, blue) in rBM-MSCs cultured on the two types of nanocomposite membranes for 3 and 6 h. b) Quantitative analysis of the averaged cytoskeleton area per cell after 3 and 6 h of culture. c) Quantitative analysis of the cell aspect ratio after 3 and 6 h of culture. d) Quantitative analysis of the whole FA area per cell after 3 and 6 h of culture. e) Quantitative analysis of the single mature FA area after 3 and 6 h of culture. f) Correlative analysis of total FA area/cell spreading area after 3 and 6 h of culture. Data trends are plotted and compared with the linear least squares fitting (light blue and dark yellow lines, slope values are indicated). (NS, not significant; $^{**}p < 0.01$ and $^{***}p < 0.001$)

**ADVANCED
SCIENCE NEWS**

www.advancedsciencenews.com

**ADVANCED
MATERIALS**

www.advmat.de

Figure 4. Heterogeneous surface potential enhances osteogenic differentiation and mineralization of BM-MSCs. a) Representative immunofluorescence staining images of the osteogenic protein markers BMP-2 and OPN (green) in rBM-MSCs cultured on the BTO/P(VDF-TrFE) membranes for 3 and 7 days, respectively. DAPI and phalloidin were used to stain cell nuclei (blue) and F-actin (red), respectively. b) Quantitative analysis of the fluorescence intensities of BMP-2 and OPN expression in rBM-MSCs cultured on the BTO/P(VDF-TrFE) membranes for 3 and 10 days, respectively. c) Hierarchical cluster analysis of key differentially-expressed osteogenesis-related genes at the 3 and 7days timepoints. d) mRNA expression levels of representative osteogenic genes (BMP-2, TNC, OCN) in BM-MSCs after culture for 3 and 7 days. e) Representative Alizarin Red S staining images of rBM-MSCs cultured on the BTO/P(VDF-TrFE) membranes for 21 days. The insets showed the macroscopic images. f) The quantitative analysis of Alizarin Red S staining. ($^{*}p < 0.05$ and $^{**}p < 0.01$ and $^{***}p < 0.001$)

on the BTNF substrates is significantly lower than that on the BTNP substrate surfaces at both 3 and 6 h, which was also consistent with the cell morphology observation. Furthermore, cells cultured on the BTNF substrates developed significantly larger-sized focal adhesions (FAs) (3.65 ± 2.56 μm^2 on BTNF vs 2.16 ± 0.55 μm^2 on BTNP) that displayed more intense staining against vinculin, a key adaptor protein of FAs (Figure 3a,e). This difference was also confirmed by quantitative analysis of the total FA area (Figure 3d) and correlative analysis of total FA area/cell spreading area (Figure 3f). The size of the FAs has been shown to be proportional to the magnitude of the traction force applied to the FAs by the cells.[22] Therefore, we can calculate that the tensile stress associated with a single mature FA on the BTNF and BTNP substrates after 6 h are ≈20.07 and 11.88 nN, respectively, based on the constant stress force applied at the FA of 5.5 ± 2 nN μm^{-2}.[23] This indicates that the heterogeneous surface potential microenvironment mediated by BTNF membranes exerts a strong traction force on BM-MSCs and causes the cells to produce a distinct tensile response, which may trigger subsequent functional differentiation through mechanical transduction. These findings thus further confirm the role of heterogeneous surface potential in modulating BM-MSCs behavior. We

hypothesize that the BTNF substrates can essentially serve as an artificial heterogeneous surface potential microenvironment platform to regulate the adhesion, spreading and functional activity of BM-MSCs.

2.5. Heterogeneous Surface Potential Enhances Osteogenic Differentiation and Mineralization of BM-MSCs In Vitro

We next examined the effects of heterogeneous surface electric potential of the BTNF substrates on the osteogenic differentiation of BM-MSCs without chemical-inducing agents, after excluding the interference of unpolarized BTNF membrane surface structure (Figure S10, Supporting Information). Compared to the control BTNP substrates, BTNF substrates with heterogeneous surface potential exhibited significantly higher expression of BMP-2 on day 3 and OPN on day 7, as seen from the immunofluorescence analysis data (**Figure 4**a,b), which indicated that stem cell osteogenesis is enhanced by heterogeneous distribution of surface potential on the artificial ECM microenvironment mediated by BTNF substrates.

To further investigate differential gene expression of BM-MSCs elicited by varying surface electric potential distribution, we performed a global microarray gene analysis. The principal component analysis (PCA) results confirmed the presence of sub-populations with distinct transcriptomes (Figure S11a, Supporting Information). Based on the differentially expressed genes ($p<0.05$), heat maps generated by hierarchical clustering revealed that there was a significant difference in the mRNAs expression profiles between the BTNF and BTNP group, and the number of upregulated genes in BM-MSCs cultured on BTNF, increased from day 3 to day 7 (Figure S11b,c, Supporting Information). Hierarchical clustering analysis showed that a panel of gene transcripts associated with osteogenic differentiation, particularly the intermediate and late-stage osteogenic markers (BMP-2, SPP1, ANKH, and TNC) were upregulated in the BTNF matrix, as compared with the BTNP matrix on both day 3 and day 7 (Figure 4c). The RT-qPCR results of representative osteogenic genes also confirmed this trend (Figure 4d). Subsequently, we examined whether heterogeneous surface potential can induce high levels of mineralization in BM-MSCs. As shown in Figure 4e, abundant mineralization nodules were induced on BTNF substrates after 21 days of co-culture, as detected by alizarin red staining, which was also confirmed by quantitative analysis of ECM mineralization (Figure 4f). All these findings thus suggest that heterogeneous surface potential distribution on BTNF substrates strongly promotes osteogenic differentiation of BM-MSCs in vitro. We hypothesize that this heterogeneous surface potential pattern produces a special stimulus to enhance the osteogenic differentiation of BM-MSCs.
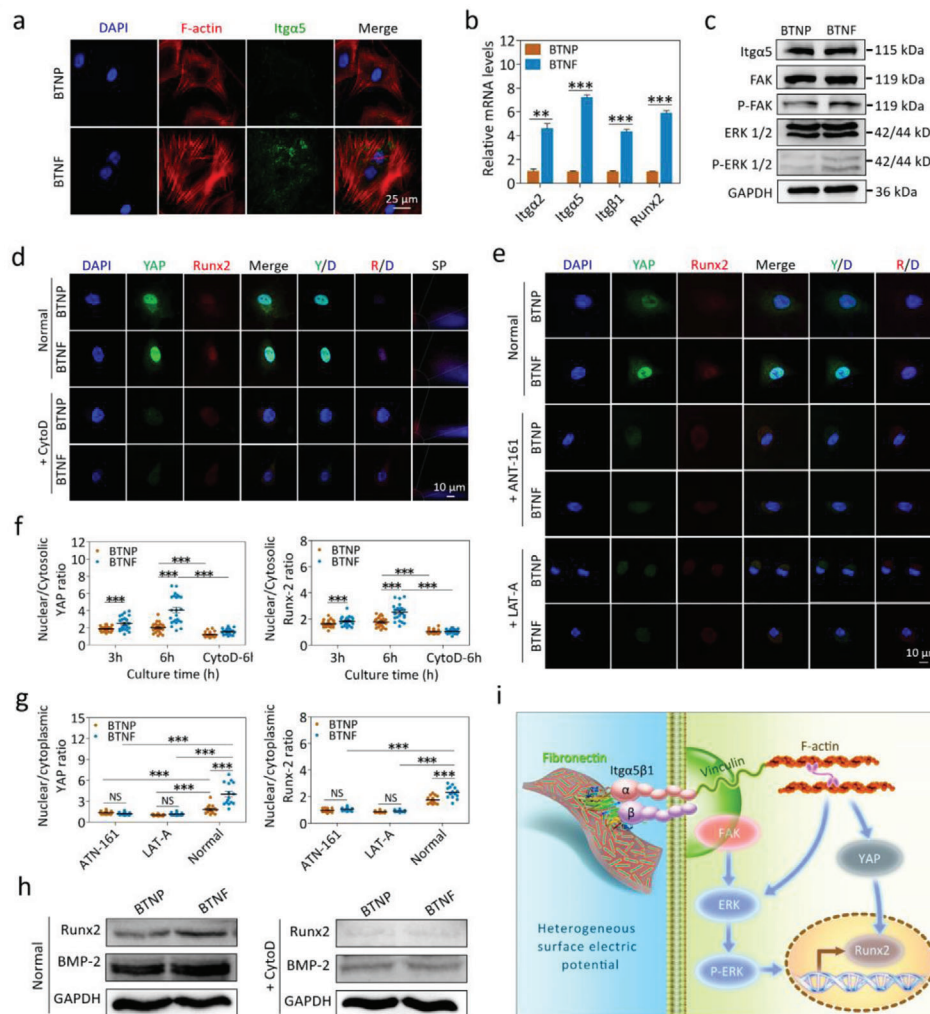
2.6. Heterogeneous Surface Potential Promotes Osteogenesis by Amplifying Cellular Mechanosensing

In view of the superiority of heterogeneous surface potential distribution in promoting cytoskeletal organization, focal adhesion maturation, cytoskeletal traction force enhancement and osteogenic differentiation of BM-MSCs, we further explored the underlying mechanisms by which physical cues associated with surface potential heterogeneity are transduced into intracellular chemical signals. To the best of our knowledge, the exact sequence of signaling events and molecular mechanisms associated with surface potential heterogeneity-mediated osteogenesis have not yet been investigated. Accumulated evidence in the scientific literature has pointed to $\alpha5\beta1$ integrin signaling playing an important role during the osteogenic differentiation of MSCs mediated by substrate physical properties, such as stiffness and surface topology structure.[24] In this study, we observed more intense immunofluorescence staining (**Figure 5**a) and more abundant protein synthesis (Figure 5c) of integrin $\alpha5$ (Itg$\alpha5$) on the BTNF versus BTNP substrate, after 6 h of culture. The qPCR results showed significantly upregulated expression of integrin genes (Itg $\alpha2$, $\alpha5$, and $\beta1$) on the BTNF membranes after 6 h of culture, which was also positively correlated with expression of the upstream osteogenic differentiation transcription factor Runx2 (Figure 5b). These results may be attributed to increased cytoskeletal organization and enhanced cell spreading on the BTNF versus BTNP substrate surface as mentioned above. Previous studies showed that integrins $\alpha5$ and

$\beta1$ were associated with basal cytoskeletal F-actin structures.[25] Downregulation of Itg$\alpha5$ using specific chemical agents (ANT-161) suppressed osteogenic differentiation, such as Runx2 expression (Figure 5e). These results suggest that surface potential heterogeneity and Itg$\alpha5$ clustering act in concert to promote osteogenic differentiation of BM-MSCs, which would imply that physical stimulation through heterogeneous surface potential enhance BM-MSC osteogenic differentiation by amplifying cellular mechanosensing. It has previously been shown that the process of integrin-mediated mechanotransduction involves activation of the extracellular signal-regulated kinase (ERK)1/2 and focal adhesion kinase (FAK) signaling pathways.[26] Therefore, we confirmed the activation of these signaling pathways by performing western blot analysis on ERK, phosphorylated ERK 1/2 (pERK 1/2), FAK, and pFAK protein expression (Figure 5c). There were obvious increases in the expression levels of pERK 1/2 and pFAK on BTNF versus BTNP. Hence, the heterogeneous presentation of surface potential promotes the activation of mechanosensing pathways by upregulating integrin expression and enhancing mechanotransduction-dependent differentiation of stem cells.

Next, we investigated how heterogeneous electrical stimulation signals are transduced into intracellular signaling pathways by integrin-mediated mechanotransduction to promote osteogenic differentiation of BM-MSCs. It is well-known that Yes-associated protein (YAP) is a major downstream effecter of the Hippo pathway and partners with the TEAD family of transcription factors to activate mechanotransduction that promote osteogenic differentiation of stem cells.[27] In our study, the heterogeneous surface potential pattern enhances nuclear translocation of YAP and Runx2 (Figure 5d), which in turn induces early osteogenic differentiation of BM-MSCs. The quantitative analysis of both the nuclear/cytoplasmic ratio of YAP and the nuclear accumulation of Runx2 showed that BTNF significantly enhanced the nuclear accumulation of YAP/Runx2 as compared to BTNP ($p < 0.001$) (Figure 5f). These results thus suggest that heterogeneous surface potential could amplify mechanosensing in BM-MSCs and promote the early entry of YAP into the nucleus, thereby initiating the expression of upstream osteogenic-related markers, such as Runx2.
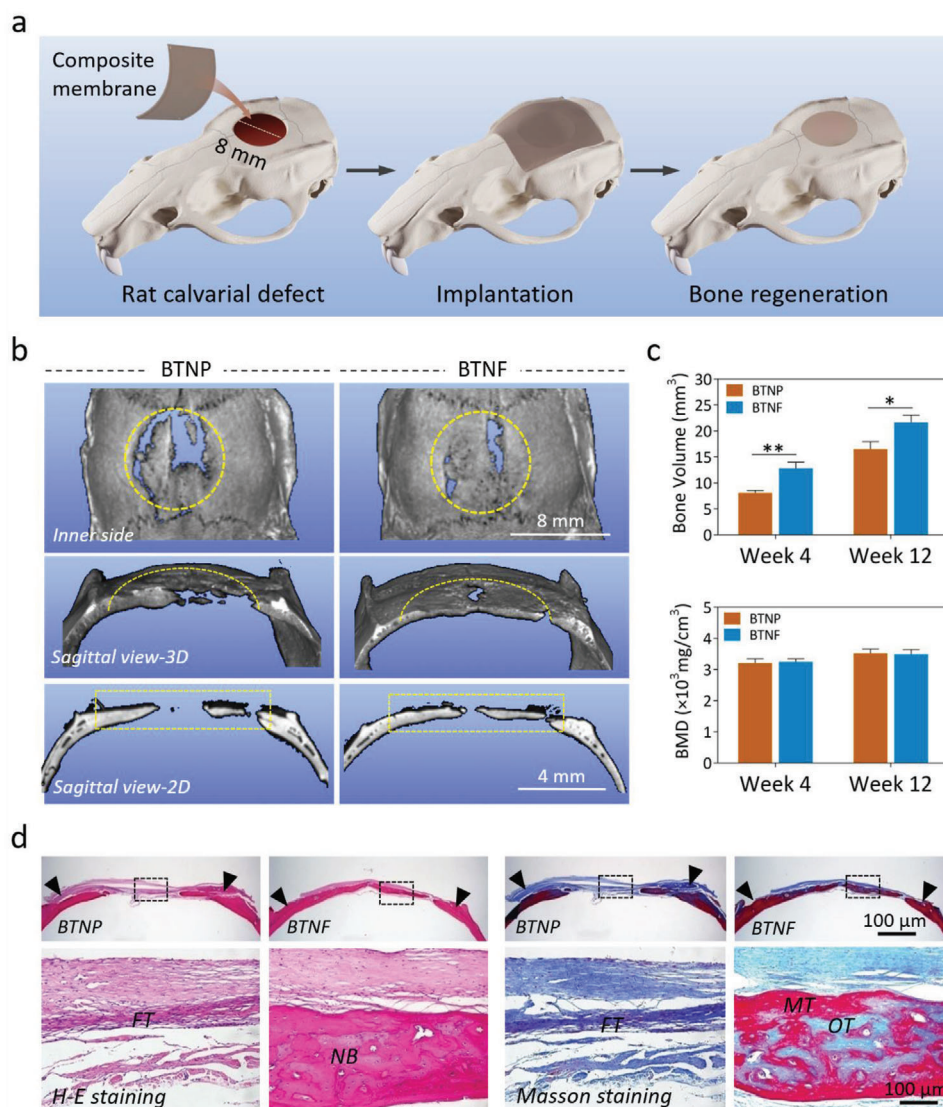
After determining that heterogeneous surface potential can promote osteogenic differentiation of BM-MSCs by accelerating nuclear translocation of YAP/Runx2, we further investigated the cellular mechanosensing pathway mediated by heterogeneous surface potential. First, we investigated the role of integrins in regulating YAP-mediated mechanosensing of heterogeneous surface potential. Downregulating Itg$\alpha5$ with specific chemical agents, such as ANT-161 significantly decreased YAP nuclear localization (Figure 5e) and weakened early osteogenic differentiation of BM-MSCs (Figure 5g). This result suggests that transmembrane receptor integrins play a crucial role in YAP nuclear localization during osteogensis mediated by heterogeneous surface electrical potential. Then, we examined the role of cytoskeletal F-actin on YAP/Runx2 nuclear localization during heterogeneous electrical stimulation. Cytochalasin D treatment (to inhibit cytoskeletal organization) demonstrated the key roles of cytoskeletal organization in mechanotransduction (Figure 5d) and osteogenesis (Figure 5h). These results are consistent with previous studies which showed that stretching of organized

**ADVANCED
SCIENCE NEWS**

www.advancedsciencenews.com

**ADVANCED
MATERIALS**

www.advmat.de

Figure 5. Heterogeneous surface potential enhances osteogenesis by amplifying cellular mechanosensing. a) Immunofluorescence staining images of integrin α5 (Itgα5, green) expression in rBM-MSCs cultured on the BTO/P(VDF-TrFE) membranes after 6 h. DAPI and phalloidin were used to stain cell nuclei (blue) and F-actin (red), respectively. b) mRNA expression levels of representative integrin genes (Itgα2, Itgα5, and Itgβ1) and osteogenic gene (Runx2) in BM-MSCs after 6 h of culture. c) Western blot analysis of Itgα5, FAK, phospho-FAK, ERK 1/2, and phospho-ERK1/2 (Thr202/Tyr204) protein expression in rBM-MSCs cultured on the nanocomposite membranes after 6 h. d) Representative immunofluorescence staining images of YAP and Runx2 nuclear translocation in normal culture medium and medium supplemented with Cytochalasin D, respectively. (DAPI, blue; YAP, green; Runx2, red; Y/D, YAP/DAPI; R/D, Runx2/DAPI; SP, Scatter plot). e) Representative immunofluorescence staining images of YAP and Runx2 nuclear translocation in normal culture medium and medium supplemented with Integrin α5β1 Inhibitor ATN-161 or nuclear pore inhibitor LAT-A (YAP, green; Runx2, red; DAPI, blue; Y/D, YAP/DAPI; R/D, Runx2/DAPI). f) Quantitative analysis of nuclear/cytosolic YAP and Runx2 ratios in rBM-MSCs cultured on the nanocomposite membranes after 3 and 6 h. g) Quantitative analysis of nuclear/cytosolic YAP and Runx2 ratios in rBM-MSCs cultured on nanocomposite membranes after LAT-A and ATN-161 treatment. h) Western blot analysis of Runx2 and BMP-2 protein expression in rBM-MSCs cultured on the nanocomposite membranes after 6 h. i) A schematic representation of molecular signaling events that mediates heterogeneous surface potential-induced BM-MSC osteogenic differentiation. (NS, no significant; $^{**}p < 0.01$ and $^{***}p < 0.001$).

cytoskeletal fibers can enlarge nuclear pores to facilitate the nuclear transfer of YAP, thereby indicating a positive effect of cytoskeletal organization on osteogenesis.[28] To further investigate whether such enlarged nuclear pores stretched by organized cytoskeletal fibers facilitate YAP nuclear localization, we used the nuclear actin inhibitor LAT-A to block the nuclear membrane and found that YAP nuclear localization and Runx2 expression decreased significantly (Figure 5e). Therefore, we propose that the heterogeneous surface electric potential microenvironment enhances BM-MSC osteogenic differentiation through amplifying Itgα5-mediated mechanosensing and downstream mechanotransduction events, which involves cell adhesion, spreading, cytoskeletal reorganization, FAK/ERK signaling cascades, nuclear pore enlargement, and YAP/Runx2 nuclear translocation (Figure 5i). The trigger for this signaling cascade may be the surface electric potential heterogeneity itself, which promotes the heterogeneous adsorption mode of ECM proteins, such as FN, thereby stimulating increased integrin clustering and FA formation, which in turn enhances osteogenesis via increased cell adhesion and spreading. Taken together, our results therefore

**ADVANCED
SCIENCE NEWS**

www.advancedsciencenews.com

**ADVANCED
MATERIALS**

www.advmat.de

Figure 6. Heterogeneous surface electric potential accelerates bone regeneration in vivo. a) Schematic representation of BTO/P(VDF-TrFE) nanocomposite membrane implantation in the bone defect area. b) Representative micro-CT images and sagittal view images of critical-sized rat calvarial full-thickness defects at 12 weeks post-implantation. Yellow dotted lines denote the boundary between nascent bone and host bone. The yellow dotted rectangle frames denote the regenerated new bone. c) Quantitative analysis of bone volume and bone mineral density (BMD) ($^*p < 0.05$, $^{**}p < 0.01$). d) H&E staining and Masson's trichrome staining of histological sections at 12 weeks after implantation. (NB, nascent bone; FT, fibrous tissue; OT, osteoid tissue; MT, mineralized tissue).

identified surface potential heterogeneity as a new key property of biomaterials that influence osteogenic differentiation of stem cells.

2.7. Heterogeneous Surface Electric Potential Accelerates Bone Regeneration In Vivo

We finally evaluated whether the heterogeneous surface electric potential microenvironment can accelerate bone defect repair. Polarized BTNF membranes were implanted to cover freshly-formed 8 mm supercritical-sized calvarial defects in mature rats. Bone growth was evaluated at 4 and 12 weeks after implanta-

tion. Gross observation indicated conspicuous nascent bone formation within the defect site after 4 weeks and almost complete bone defect healing after 12 weeks at sites covered with the BTNF membranes, as compared with BTNP membranes (Figure S12, Supporting Information). As evidenced by micro-CT analysis, the defect was filled with homogeneous and contiguously regenerated mature bone when covered with BTNF membranes for 12 weeks (**Figure 6**b), as well as 4 weeks (Figure S14, Supporting Information). As expected, micro-CT analysis showed that the polarized BTNF membranes led to a substantial increase in the amount of regenerated bone volume, even though there was no significant difference in the bone mineral density (BMD) between the BTNF and BTNP groups during implantation

**ADVANCED
SCIENCE NEWS**

www.advancedsciencenews.com

**ADVANCED
MATERIALS**

www.advmat.de

(Figure 6c). As evidenced by X-ray detection, the nascent bone is indistinguishable from the surrounding host bone after implantation of the polarized BTNF membranes for 12 weeks (Figure S13, Supporting Information).

Histological analysis revealed that the polarized BTNF membranes facilitated improved new bone formation that led to almost complete healing with flat and contiguous bone-structure formation and full bone maturity after 12 weeks implantation, as seen from the H-E staining images. By contrast, in the polarized BTNP membranes group, there was a lack of complete and continuous healing with regenerated host tissues appearing only when the observation time was extended to 12 weeks (Figure 6d). Further analysis with Masson's trichrome staining revealed that mature osteoid tissue was present within the central region of the defect after 12 weeks implantation of the polarized BTNF membranes, whereas a large amount of fibrous connective tissue still occupied the center of the defect implanted with BTNP membrane (Figure 6d). These results thus indicate that polarized BTNF composite membranes can accelerate the supercritical-sized calvarial defect repair process through maintenance of a heterogeneous electrical microenvironment.

3. Conclusion

This study demonstrates that the heterogeneous distribution of surface potential on BTNF/P(VDF-TrFE) nanocomposite membrane could be achieved by switching from BTO nanospheres to BTO nanofibers and optimizing the aspect ratios of BTNF fillers. Furthermore, our work indicates that intracellular mechanotransduction mediated by changes in cytoskeletal organization and YAP/Runx2 nuclear translocation within BM-MSCs could be the underlying mechanisms by which heterogeneous distribution of surface electric potential promotes osteogenesis. Consequently, the membranes with heterogeneous surface electric potential enhance bone regeneration in vivo. Our findings thus suggest that surface potential heterogeneity at the micro- and nanoscale should be considered a key parameter in biomaterial design, which might provide a new strategy for tissue regenerative therapies.

Supporting Information

Supporting Information is available from the Wiley Online Library or from the author.

Conflict of Interest

The authors declare no conflict of interest.

Data Availability Statement

The data that support the findings of this study are available in the supplementary material of this article.

[1] a) X. Yao, R. Peng, J. D. Ding, *Adv. Mater.* **2013**, *25*, 5257; b) J. H. Wen, L. G. Vincent, A. Fuhrmann, Y. S. Choi, K. C. Hribar, H. Taylor-Weiner, S. Chen, A. J. Engler, *Nat. Mater.* **2014**, *13*, 979; c) P. Viswanathan, M. G. Ondeck, S. Chirasatitsin, K. Ngamkham, G. C. Reilly, A. J. Engler, G. Battaglia, *Biomaterials* **2015**, *52*, 140; d) X. H. Zhang, C. G. Zhang, Y. H. Lin, P. H. Hu, Y. Shen, K. Wang, S. Meng, Y. Chai, X. H. Dai, X. Liu, Y. Liu, X. J. Mo, C. Cao, S. Li, X. L. Deng, L. L. Chen, *ACS Nano* **2016**, *10*, 7279; e) T. Razafiarison, C. N. Holenstein, T. Stauber, M. Jovic, E. Vertudes, M. Loparic, M. Kawecki, L. Bernard, U. Silvan, J. G. Snedeker, *Proc. Natl. Acad. Sci. USA* **2018**, *115*, 4631.

[2] A. K. Capulli, L. A. MacQueen, S. P. Sheehy, K. K. Parker, *Adv. Drug Delivery Rev.* **2016**, *96*, 83.

[3] a) M. J. Dalby, N. Gadegaard, R. Tare, A. Andar, M. O. Riehle, P. Herzyk, C. D. W. Wilkinson, R. O. C. Oreffo, *Nat. Mater.* **2007**, *6*, 997; b) D. Y. Lu, C. H. Luo, C. Zhang, Z. Li, M. Long, *Biomaterials* **2014**, *35*, 3945; c) J. Zhang, X. He, S. Lin, X. Chen, L. Dong, J. Lin, H. Wang, W. Weng, K. Cheng, *Adv. Mater. Interfaces* **2022**, *9*, 2102549.

[4] a) M. Mehrali, A. Thakur, C. P. Pennisi, S. Talebian, A. Arpanaei, M. Nikkhah, A. Dolatshahi-Pirouz, *Adv. Mater.* **2017**, *29*, 1603612; b) V. R. Feig, H. Tran, M. Lee, Z. A. Bao, *Nat. Commun.* **2018**, *9*, 2740; c) G. Anand, A. Lowe, A. Al-Jumaily, *Mater. Sci. Eng., C* **2019**, *96*, 496.

[5] a) A. S. Motamedi, H. Mirzadeh, F. Hajiesmaeilbaigi, S. Bagheri-Khoulenjani, M. A. Shokrgozar, *J. Biomed. Mater. Res., Part A* **2017**, *105*, 1984; b) M. Kitsara, A. Blanquer, G. Murillo, V. Humblot, S. D. Vieira, C. Nogues, E. Ibanez, J. Esteve, L. Barrios, *Nanoscale* **2019**, *11*, 8906; c) Y. S. Lee, G. Collins, T. L. Arinzeh, *Acta Biomater.* **2011**, *7*, 3877; d) Y. S. Lee, S. L. Wu, T. L. Arinzeh, M. B. Bunge, *Biotechnol. Bioeng.* **2017**, *114*, 444; e) S. L. Wu, M. S. Chen, P. Maurel, Y. S. Lee, M. B. Bunge, T. L. Arinzeh, *J. Neural Eng.* **2018**, *15*, 056010.

[6] a) Y. Zhang, L. J. Chen, J. Zeng, K. C. Zhou, D. Zhang, *Mater. Sci. Eng., C* **2014**, *39*, 143; b) A. Marino, J. Barsotti, G. de Vito, C. Filippeschi, B. Mazzolai, V. Piazza, V. Labardi, V. Mattoli, G. Ciofani, *ACS Appl. Mater. Interfaces* **2015**, *7*, 25574; c) A. V. Zanfir, G. Voicu, C. Busuioc, S. I. Jinga, M. G. Albu, F. Iordache, *Mater. Sci. Eng., C* **2016**, *62*, 795.

[7] a) J. H. Li, X. N. Mou, J. C. Qiu, S. Wang, D. Z. Wang, D. H. Sun, W. B. Guo, D. S. Li, A. Kumar, X. B. Yang, A. X. Li, H. Liu, *Adv. Healthcare Mater.* **2015**, *4*, 998; b) J. H. Li, J. C. Qiu, W. B. Guo, S. Wang, B. J. Ma, X. N. Mou, M. Tanes, H. D. Jiang, H. Liu, *Nanoscale* **2016**, *8*, 7416.

[8] a) P. Yu, C. Ning, Y. Zhang, G. Tan, Z. Lin, S. Liu, X. Wang, H. Yang, K. Li, X. Yi, Y. Zhu, C. Mao, *Theranostics* **2017**, *7*, 3387; b) J. Q. Chen, W. P. Li, L. Zhou, Z. N. Zhou, G. X. Tan, D. F. Chen, R. X. Wang, P. Yu, C. Y. Ning, *J. Mater. Chem. B* **2018**, *6*, 2723; c) T. Yao, J. Chen, Z. Wang, J. Zhai, Y. Li, J. Xing, S. Hu, G. Tan, S. Qi, Y. Chang, P. Yu, C. Ning, *Colloids Surf., B* **2019**, *175*, 463.

[9] a) D. Kai, M. P. Prabhakaran, G. Jin, S. Ramakrishna, *J. Biomed. Mater. Res., Part A* **2011**, *99*, 376; b) S. Hinderer, S. L. Layland, K. Schenke-Layland, *Adv. Drug Delivery Rev.* **2016**, *97*, 260.

**ADVANCED
SCIENCE NEWS**

www.advancedsciencenews.com

**ADVANCED
MATERIALS**

www.advmat.de

[10] X. H. Zhang, Y. H. Ma, C. W. Zhao, W. T. Yang, *Appl. Surf. Sci.* **2014**, *305*, 531.

[11] a) Z. H. Shen, J. J. Wang, J. Y. Jiang, Y. H. Lin, C. W. Nan, L. Q. Chen, Y. Shen, *Adv. Energy Mater.* **2018**, *8*, 1800509; b) Z. H. Shen, J. J. Wang, Y. H. Lin, C. W. Nan, L. Q. Chen, Y. Shen, *Adv. Mater.* **2018**, *30*, 1704380; c) Z. H. Shen, J. J. Wang, J. Y. Jiang, S. X. Huang, Y. H. Lin, C. W. Nan, L. Q. Chen, Y. Shen, *Nat. Commun.* **2019**, *10*, 1843.

[12] R. Dehghani, N. Bidabadi, M. M. Hosseini, *J. Interdiscip. Math.* **2019**, *22*, 75.

[13] M. Arbatti, X. B. Shan, Z. Y. Cheng, *Adv. Mater.* **2007**, *19*, 1369.

[14] M. F. Guo, J. Y. Jiang, Z. H. Shen, Y. H. Lin, C. W. Nan, Y. Shen, *Mater. Today* **2019**, *29*, 49.

[15] a) A. Kotwal, C. E. Schmidt, *Biomaterials* **2001**, *22*, 1055; b) M. Rahmati, M. Mozafari, *Mater. Today Commun.* **2018**, *17*, 527.

[16] T. Guo, W. Kang, D. Xiao, R. Duan, W. Zhi, J. Weng, *Molecules* **2013**, *19*, 149.

[17] F. Kimizuka, Y. Ohdate, Y. Kawase, T. Shimojo, Y. Taguchi, K. Hashino, S. Goto, H. Hashi, I. Kato, K. Sekiguchi, K. Titani, *J. Biol. Chem.* **1991**, *266*, 3045.

[18] a) A. C. Brown, J. A. Rowe, T. H. Barker, *Tissue Eng., Part A* **2011**, *17*, 139; b) J. C. Friedland, M. H. Lee, D. Boettiger, *Science* **2009**, *323*, 642; c) A. Krammer, D. Craig, W. E. Thomas, K. Schulten, V. Vogel, *Matrix Biol.* **2002**, *21*, 139.

[19] C. Halperin, S. Mutchnik, A. Agronin, M. Molotskii, P. Urenski, M. Salai, G. Rosenman, *Nano Lett.* **2004**, *4*, 1253.

[20] S. H. D. Wong, B. H. Yin, B. G. Yang, S. E. Lin, R. Li, Q. Feng, H. R. Yang, L. Zhang, Z. M. Yang, G. Li, C. H. J. Choi, L. M. Bian, *Adv. Funct. Mater.* **2019**, *29*, 1806822.

[21] a) M. M. Pathak, J. L. Nourse, T. Tran, J. Hwe, J. Arulmoli, D. T. T. Le, E. Bernardis, L. A. Flanagan, F. Tombola, *Proc. Natl. Acad. Sci. USA* **2014**, *111*, 16148; b) K. H. Vining, D. J. Mooney, *Nat. Rev. Mol. Cell Biol.* **2017**, *18*, 728.

[22] a) B. Geiger, J. P. Spatz, A. D. Bershadsky, *Nat. Rev. Mol. Cell Biol.* **2009**, *10*, 21; b) L. Trichet, J. L. Digabel, R. J. Hawkins, R. K. Vedula, M. Gupta, C. Ribrault, P. Hersen, R. Voituriez, B. Ladoux, *Proc. Natl. Acad. Sci. USA* **2012**, *109*, 6933.

[23] N. Q. Balaban, U. S. Schwarz, D. Riveline, P. Goichberg, G. Tzur, I. Sabanay, D. Mahalu, S. Safran, A. Bershadsky, L. Addadi, B. Geiger, *Nat. Cell Biol.* **2001**, *3*, 466.

[24] a) F. M. Watt, W. T. Huck, *Nat. Rev. Mol. Cell Biol.* **2013**, *14*, 467; b) M. J. Dalby, N. Gadegaard, R. O. C. Oreffo, *Nat. Mater.* **2014**, *13*, 558; c) Z. Sun, M. Costell, R. Fassler, *Nat. Cell Biol.* **2019**, *21*, 25.

[25] a) M. Vicente-Manzanares, C. K. Choi, A. R. Horwitz, *J. Cell Sci.* **2009**, *122*, 199; b) J. Z. Kechagia, J. Ivaska, P. Roca-Cusachs, *Nat. Rev. Mol. Cell Biol.* **2019**, *20*, 457.

[26] a) M. A. Schwartz, *Cold Spring Harbor Perspect. Biol.* **2010**, *2*, a005066. b) K. A. Jansen, P. Atherton, C. Ballestrem, *Semin. Cell Dev. Biol.* **2017**, *71*, 75; c) Y. Wei, S. J. Jiang, M. T. Si, X. H. Zhang, J. Y. Liu, Z. Wang, C. Cao, J. Y. Huang, H. B. Huang, L. L. Chen, S. T. Wang, C. L. Feng, X. L. Deng, L. Jiang, *Adv. Mater.* **2019**, *31*, 1900582.

[27] H. Pan, Y. Xie, Z. Zhang, K. Li, D. Hu, X. Zheng, Q. Fan, T. Tang, *Colloids Surf., B* **2017**, *152*, 344.

[28] a) C. Yang, M. W. Tibbitt, L. Basta, K. S. Anseth, *Nat. Mater.* **2014**, *13*, 645; b) A. Elosegui-Artola, I. Andreu, A. E. M. Beedle, A. Lezamiz, M. Uroz, A. J. Kosmalska, R. Oria, J. Z. Kechagia, P. Rico-Lastres, A. L. Le Roux, C. M. Shanahan, X. Trepat, D. Navajas, S. Garcia-Manyes, P. Roca-Cusachs, *Cell* **2017**, *171*, 1397.